CO_2 adsorption on pure and oxidized Ni nano-structures deposited on mica surfaces

K. W. B. Hunvik, B. Pacáková, and S. Raaen

Department of Physics, Norwegian University of Science and Technology, NTNU, 7491 Trondheim, Norway

ARTICLE HISTORY

Compiled February 24, 2021

ABSTRACT

Adsorption and desorption of CO_2 on metallic and oxidized Ni nano-structures supported on mica (muscovite) substrates have been studied by temperature programmed desorption (TPD), X-ray photoelectron spectroscopy (XPS) and atomic force microscopy (AFM). Predominantly physisorption was observed at low temperatures near 130 K. Weak desorption features where found at temperatures up to about room temperature for both metallic and oxidized samples. No clear indication of dissociation of CO_2 was found on neither the oxidized nor the metallic sample. More CO_2 was observed to adsorb on oxidized Ni nano-structures as compared to the metallic structures. A large affinity to adsorption of CO from the ambient vacuum was seen on the nano-structures. An absence of strong dependence on Ni amount on CO_2 adsorption is reported.

CONTACT S. Raaen. Email: sraaen@ntnu.no

1. Introduction

Carbon dioxide is the most abundant green house gas, and therefore studies of adsorption characteristics may be of considerable environmental relevance. Furthermore, CO_2 chemistry is of technological interest in heterogeneous catalytic processes [1, 2], and is important for the organic synthesis of chemicals like methanol, which is a promising candidate as energy carrier for fuel cells and internal combustion engines [3, 4]. A previous work on the Ni/Cu(100) system found that the turnover frequency for CO_2 hydrogenation was 60 times higher at Ni sites as compared to Cu sites [5, 6]. The promoting role of Ni and the interaction between CO_2 with Ni and other transition metal surfaces are not completely understood.[7] Previous reports suggest that Ni(110) is the only transition metal low Miller index surface where CO_2 chemically binds in an ultra-high-vacuum environment without the presence of electron donor elements [8, 7, 9]. Adsorption of CO_2 on Ni surfaces may involve physisorption, chemisorption, dissociation, as well as carbonate formation. Physisorption is commonly found at low temperatures, and chemisorption is enhanced in the presence of high defect density. At higher temperatures approaching room temperature, dissociation and carbonate formation may occur [8].

Presently, adsorption and desorption of CO_2 on Ni nano-structures/nano-particles supported on substrates of muscovite mica have been considered. Nano-particles exhibit large size-dependent changes in structural and electronic properties, and size may be expected to affect strongly adsorption properties. A recent work on adsorption and desorption of carbon monoxide on nickel nano-structures on muscovite mica has shown strong dependence on nano-structure size on the desorption characteristics [10]. Nano-particles of FCC metals tend to form cubo-octahedral shapes in order to minimize the free energy [11, 12]. Recently, it was shown for cubo-octahedral clusters that for small particles the fraction of terrace sites approaches zero, whereas for clusters consisting of a few hundred atoms the fraction of terrace sites is above 50 % [13]. In the present paper, absence of strong dependence on Ni nano-structure size is reported for CO_2 adsorption on Ni deposited on mica (muscovite) surfaces. A similar conclusion was obtained in a recent work on methane adsorption on this system [14].

2. Experimental

The muscovite was obtained from Goodfellow (potassium aluminosilicate sheet, 0.15 mm thick and 12 mm diameter, condition clear ruby). The mica substrate was annealed overnight in ultra-high-vacuum (UHV) at a temperature of 700 K. Carbon contaminants were then removed by hydrogen atom bombardment using a naked filament placed in front of the sample and a hydrogen gas pressure of $2{\cdot}10^{-6}$ Torr

at sample temperature 700 K. The mica was mounted on a molybdenum support and was resistively heated. The sample could be cooled down to a temperature near 110 K. The surface structure of the cleaned mica surface was verified by low energy electron diffraction (LEED) to show a clear hexagonal pattern. Ni was deposited at the sample using e-beam deposition. A low evaporation rate of about 0.6 Å/min was used. The evaporation rate was verified by using a quartz crystal rate monitor as well as from XPS intensities. An effective thickness was obtained by considering Ni and substrate core levels. Clustering was observed during heating to 700 K. TPD spectra were obtained by using a shielded and differentially pumped Prisma quadrupole mass spectrometer (Pfeiffer). The mass spectrometer was positioned close to the sample surface during measurements to discriminate against spurious desorption from the sample support, and to obtain reproducible intensities that could be compared for different runs. Spectra were obtained from mass-to-charge ratios 2 (H_2), 18 (H_2O), 28 (CO), 32 (O_2) and 44 amu (atomic mass unit) (CO_2) simultaneously for all experimental runs. A temperature rate of 1 K/s was used for the TPD experiments. XPS measurements were recorded using a SES2002 spectrometer (Scienta) in conjunction with a monochromatized Al Kα X-ray source (Scienta). An energy resolution of about 0.4 eV was obtained at 200 eV pass energy. A flood gun was used for charge neutralization during the photoemission measurements to prevent macroscopic charges on the insulating mica substrates. AFM measurements were performed in the tapping mode in air, using a Cypher VRS microscope (Asylum Research, Oxford Instruments). Three types of probes with different resolutions have been used, namely TAP 150-G by Budget Sensors (tip radius $R < 8\,\mathrm{nm}$), SNL-10-A by Bruker probes (tip radius $R < 2\,\mathrm{nm}$) and SHR300 by Budget Sensors (tip radius $R = 1\,\mathrm{nm}$). The samples have been scanned systematically, imaging total areas of 130, 620 and 900 $\mu\mathrm{m}^2$ for individual samples. Images with large size (5×5 $\mu\mathrm{m}^2$, resolution $512 \times 512\,\mathrm{px}$) have been scanned using TAP 150-G probe, high resolution images (image size bellow 1×1 $\mu\mathrm{m}^2$, resolution $1024 \times 1024\,\mathrm{px}$) were captured using SNL-10-A and SHR300 probes. Resulting images have been processed using Gwyddion software [22], using median line leveling to determine particle/cluster diameter, surface coverage with particles/clusters, number of objects per $\mu\mathrm{m}^2$, mean square (σ_p) and mean (σ_a) roughness, and ratio of surface to projected area of objects on the mica substrate. Depending on the topography of individual samples, particles/clusters were located using the watershed algorithm or manual selection of grains with the help of edge detection algorithm [27]. The AFM images were recorded at atmospheric conditions after the TPD runs had been completed. The base pressure in the vacuum chamber was in the low 10^{-10} Torr range.

3. Results

3.1. AFM results

Ni was deposited at a substrate temperature of 150 K and the samples were subsequently heated to 700 K to finalize the formation of nano-structures. Results from AFM measurements are displayed in Fig. 1 and in the Supplementary Information File, showing the samples with 0.8, 2 and 6.4 ML coverage. The AFM images were recorded ex-situ after performing TPD and XPS measurements in-situ. The effective coverage was estimated by XPS after deposition at 150 K.

Clustering of nickel was observed upon heating to 700 K by a decrease in the XPS core level intensity ratio between Ni 2p and K 2p. In general, larger Ni depositions lead to formation of distinct nano-particles (Fig.1c and S3 and S4 in the Supplementary Information File), whereas for lower Ni depositions, more complex nano-structures were observed (Fig.1a and c and S1, S2 and S4 in the Supplementary Information File). The sample with 0.8 ML coverage exhibits similar features in all examined areas (total scanned area of 906 μm^2) – individual particles forming flat clusters in the first layer, with randomly distributed larger clusters on the top of the first layer (Fig. 1a and S1 and S4 in the Supplementary Information File). The sample with 2 ML coverage (total scanned area of 602 μm^2) displays more exotic structures formed, constituting from the homogeneous first layer of particles, with the 2^{nd} particle layer forming dendritic-like structures (Fig. 1b and S2 and S4 in the Supplementary Information File). Finally, the sample with the largest amount of deposited Ni, 6.4 ML shows a homogeneous layer of large particles touching and overlapping each other (Fig. 1c and S3 and S4 in the Supplementary Information File). Statistical parameters of each sample are summarized in Table 1. Scans of the samples with super sharp SHR300 probe having nominal tip radius of 1 nm exhibited artefact of the contrast reversal in the regions between grains (Fig. S5 and S6), manifested as sharp features. This artefact is caused by a change from attractive to repulsive mode of the cantilever, probably due to the water layer adhered between Ni grains, which causes physical catching of super-sharp spike-like probe by capillary forces [26, 24, 25]. Bearing in mind that the samples were removed from the vacuum chamber and stored in the ambient atmosphere prior to the AFM measurements, it should be noted that a distortion of the AFM images due to the hydrophilic nature of the mica substrate should occur particularly for lower Ni coverage [26, 24, 25], which has been observed (Fig. S5 and S6).

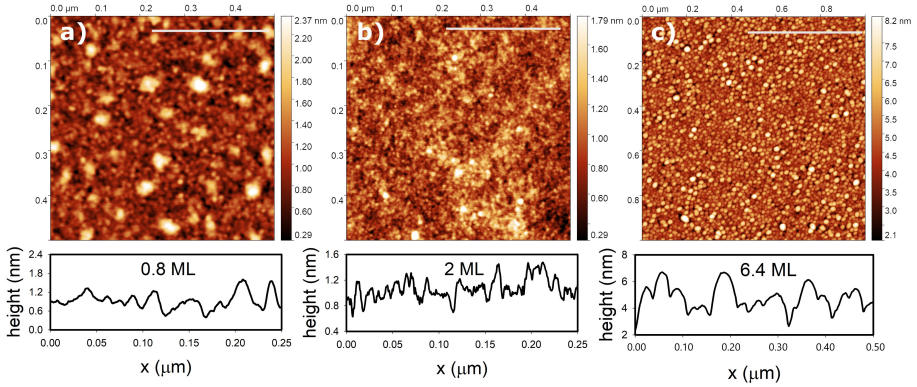

Figure 1. AFM topography images of effective coverage (a) 0.8, (b) 2.0, and (c) 6.8 ML Ni on muscovite mica, with the corresponding cross-sections bellow images. Images were captured in 1024 × 1024 px resolution using SNL-10-A probe.

Table 1. General parameters of individual samples, as determined from the AFM images. Surface coverage (%), which is the portion of mica covered with particles/grains; Grain size (nm) which represents the median size of particles/grains determined by different methods as explained in footnotes; Cluster size (nm) attributed to the median size of clusters; No. objects/μm^2 which is the average number of particles/clusters per μm^2; σ_a (nm) and σ_p (nm) representing mean and root-mean-square roughness [22, 23].

Sample	Surface coverage (%)	Grain size (nm)	Cluster size (nm)	No. objects /μm^2	σ_p [e)] (nm)	σ_a [e)] (nm)
0.8 ML	83 ± 5 *	10.1 ± 2.0 [b)] / 8.9 ± 1.5 [d)]	44 ± 14 [a)]	161 ± 30 [c)]	0.32	0.34
2 ML	85 ± 11 *	7 ± 1.5 [f)]	–	7048 ± 500	0.18	0.23
6.4 ML	100 **	24.8 ± 3	–	3400 ± 50 [e)]	0.89	0.69

* assuming the lowest parts of topography between grains/clusters can be attributed to mica, which is indirectly confirmed by water-like artefact in between grains, discussed in the Supplementary Information File

** assuming bare mica surface is not accessible, as the individual particles/grains are large and touch/overlap each other

[a)] statistics from 100 μm^2 (4 images, 5 × 5 μm^2, 1024 × 1024 px) scanned with TAP 150-G tip ($R < 8$ nm), based on watershed algorithm

[b)] based on statistics from randomly selected 116 grains, HR image (0.5 × 0.5 μm^2) scanned with SNL10-A tip ($R < 2$ nm)

[c)] clusters, statistic from 75 μm^2, scanned with TAP 150-G tip ($R < 8$ nm), based on watershed algorithm

[d)] calculated from statistics on 41 randomly selected grains, measurement from phase image with nicely distinguished grains, 0.5 × 0.2 μm^2 (Fig S7), HR probe ($R = 1$ nm)

[e)] results from 1024 × 1024 px image, 1 × 1 μm^2, taken by SNL-10A tip ($R < 2$ nm), statistics for data from total scanned area > 300 μm^2

[f)] statistics on HR image 1024 × 1024 px, 0.5 × 0.5 μm^2, watershed algorithm, SNL10-A tip

3.2. Metallic Ni nano-structures

Thermal desorption spectra of carbon dioxide were obtained from several nickel depositions on muscovite mica substrates. After Ni deposition, the samples were annealed to a temperature of 700 K before exposure to CO_2. This was done to finalize the formation of nano-structures. Figure 2 and 3 show CO_2 TPD spectra from effective Ni coverage 0.45 (bottom curve), 0.80 (middle curve), and 2.0 ML (top curve) on mica. A carbon dioxide dose of 1 L ($1\,Langmuir = 1 \cdot 10^{-6}\,Torr \cdot s$) was dosed at a substrate temperature of 130 K. These spectra are dominated by a single peak from physisorbed CO_2 at low temperature. Figure 2 shows that weak desorption structures exist in the temperature range up to about 250 K. No other distinct desorption features corresponding to mass 44 amu were observed up to a temperature of 700 K. The main desorption peaks have maximum values near temperatures 141, 135 and 158 K for effective Ni coverage 0.45, 0.80, and 2.0 ML; respectively. Corresponding spectra as in Fig.2 are shown in Fig.3 for CO (mass 28 amu). The low temperature peaks correspond to peaks in Fig.2 since CO_2 has a mass 28 amu fragmentation product. The peaks near 500 K are argued to stem from CO adsorbed on the Ni/mica sample from the background pressure in the ultra-high-vacuum chamber, since no CO_2 remains on the sample at this elevated temperature. This observation confirms the extreme affinity of CO to the supported Ni nano-structures. Fig.4 shows CO_2 TPD spectra for adsorption of 1 L CO_2 at temperatures 130, 150 and 200 K on a sample of 2.0 ML effective Ni coverage. The low temperature physisorption peak becomes smaller with increasing adsorption temperature, whereas the weak desorption features up to above 250 K are less affected. It may be noted that the physisorption peak in the bottom curve in Fig.4 appears at a temperature less than the dosing temperature of 200 K. This is thought to be caused by adsorption of residual CO_2 in the vacuum chamber as the temperature is lowered. As the temperature was ramped to 700 K increased background of the spectra were observed; however, desorption peaks were not observed in the TPD spectra in this temperature range.

XPS spectra in the binding energy region from 50 to 400 eV are shown in Fig.5 for effective Ni coverage of 0.8 (bottom spectrum) and 2.0 ML (top spectrum). The various core levels are labelled in the figure. The main differences between the two spectra are the Ni coverage and the observation of Ca 2p emission in the 2.0 ML sample. The Ca intensity was estimated to be about 10 to 15% of the Ni intensity in the XPS signal. It is noted that charge compensation was needed to prevent distortion of the core level spectra for effective Ni coverage up to at least 5 ML, which was the largest coverage that was investigated.

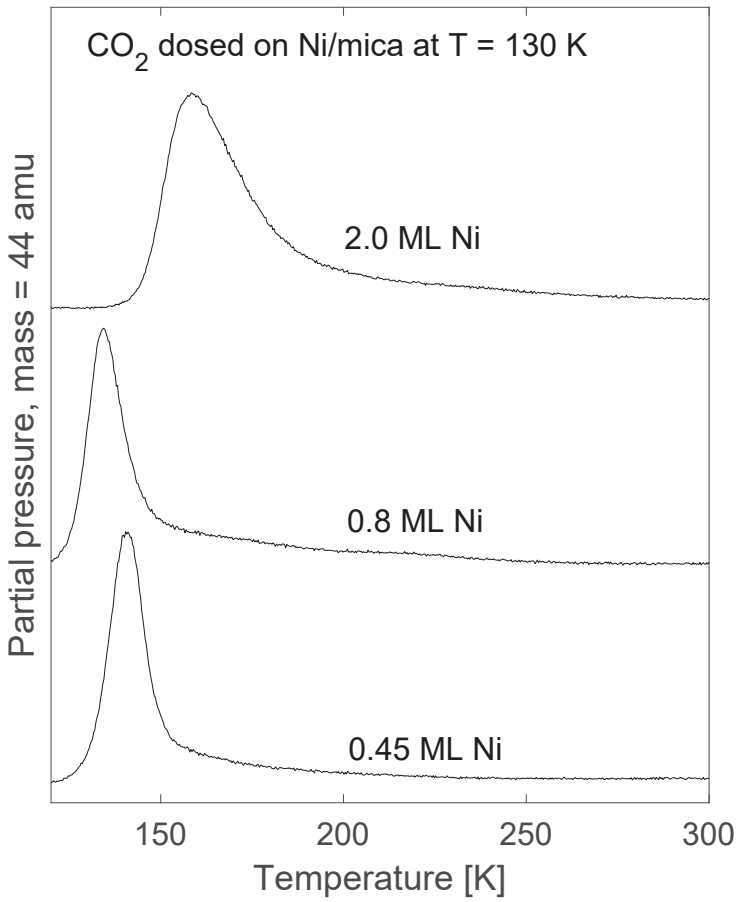

Figure 2. TPD of CO_2 (mass 44 amu). The effective Ni coverage was: 0.45 (bottom curve), 0.80 (middle curve), and 2.0 ML (top curve).

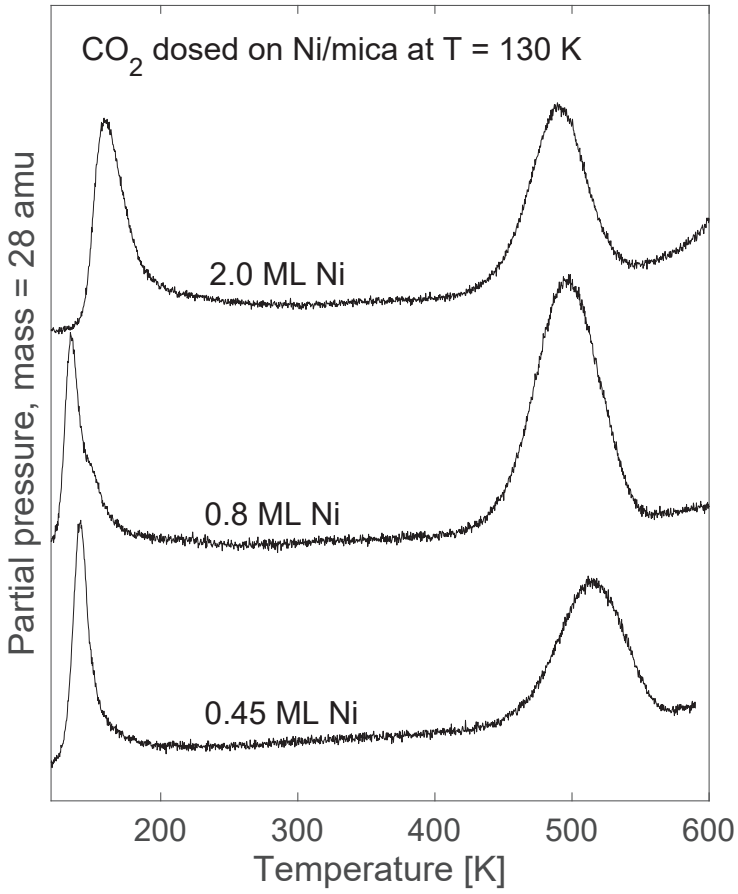

Figure 3. TPD of CO (mass 28 amu). The effective Ni coverage was: 0.45 (bottom curve), 0.80 (middle curve), and 2.0 ML (top curve).

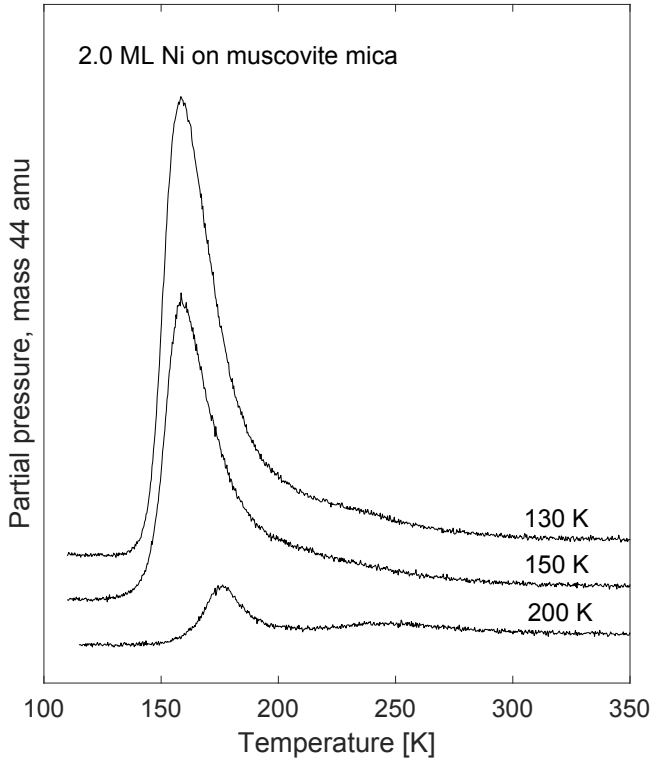

Figure 4. TPD of CO_2 (mass 44 amu) from effective Ni coverage 2.0 ML on mica.

3.3. Oxidized Ni nano-structures

Thermal desorption spectra were also obtained from oxidized Ni nano-structures on muscovite. Oxidation was performed by exposing the samples to 100 L oxygen at a temperature of 300 K. The samples were annealed to 700 K prior to the oxidation to finalize the formation of the Ni nano-structures. A comparison of desorption of CO_2 from pure and oxidized Ni nano-structures is shown in Fig.6. The exposure was from a CO_2 dose of 1 L at a substrate temperature 130 K. The top spectrum shows desorption from the oxidized sample. It is evident that more CO_2 is adsorbed on the oxidized sample. Fig.7 shows desorption of CO (mass = 28 amu) recorded simultaneously as the CO_2 spectrum. These spectra contains CO_2 fragmentation spectra in the low temperature physisorption region. The mass 28 amu peak is found near 166 K for the oxidized sample, and near 479 K for the pure metallic sample. XPS core levels for metallic and oxidized Ni on mica are shown in Fig.8 for an effective Ni coverage of 0.8 ML. The Ni shake-up satellite at about 6 eV higher binding energy with respect to the main peak is seen for both the metallic and oxidized samples [15].

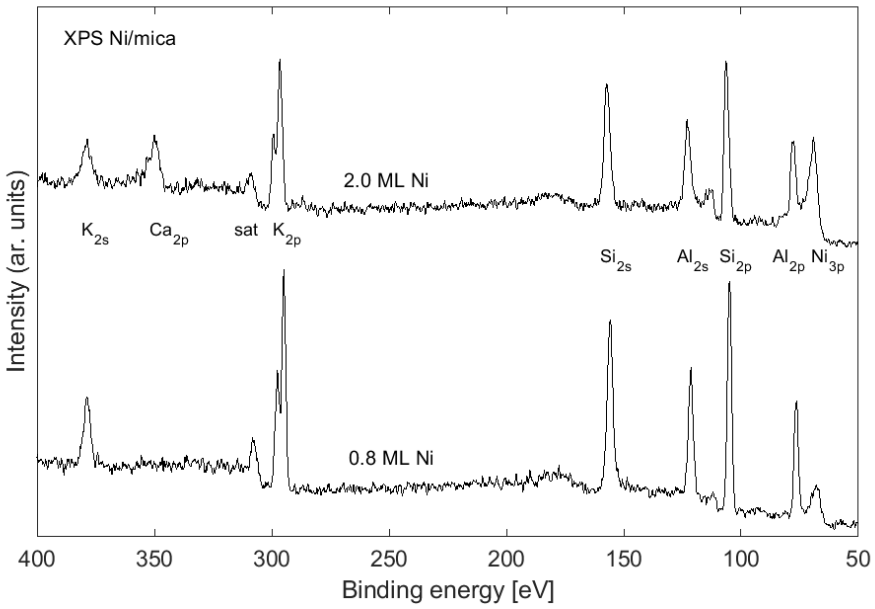

Figure 5. XPS from Ni/mica.The effective Ni coverage was 0.8 ML (bottom spectrum) and 2.0 ML (top spectrum).

4. Discussion

The AFM images show clustering of Ni atoms on the mica substrates. Mica is a weakly interacting substrate and aggregation of Ni particles are evident from the images in the supplementary file. It may be difficult to distinguish between Volmer-Weber (clustering) or Stranski-Krastanov (one or two monolayers following by clustering) growth.Aggregation of Ni atoms is temperature dependent, and the finding is that as stable structure is reached upon slow annealing of the samples to a temperature of 600 K. Peak positions in the TPD and XPS spectra were observed to depend only weakly on the amount of Ni that was deposited in the coverage range up to a few monolayers. A correlation between sample morphology and TPD and XPS spectra was thus not obtained.

The TPD spectra of CO_2 are dominated by the low temperature physisorption peak. For desorption from metallic Ni nano-structures weak features are observed near 250 K, see Fig.4. These features may possibly be attributed to chemisorption of carbon dioxide. Previous work has concluded that a low temperature chemisorption peak exists for CO_2 adsorption on Ni(110), which may be enhanced by conversion from physisorbed species by X-ray radiation in XPS experiments [19]. Presently, the desorption peaks were found to be enlarged for CO_2 adsorption on pre-oxidized Ni nano-structures, see Fig.6. The area of the desorption peaks was a factor 1.9 larger as compared to adsorption on metallic Ni. A similar enhancement was observed for the weaker desorption features at higher temperature. This suggests that more ad-

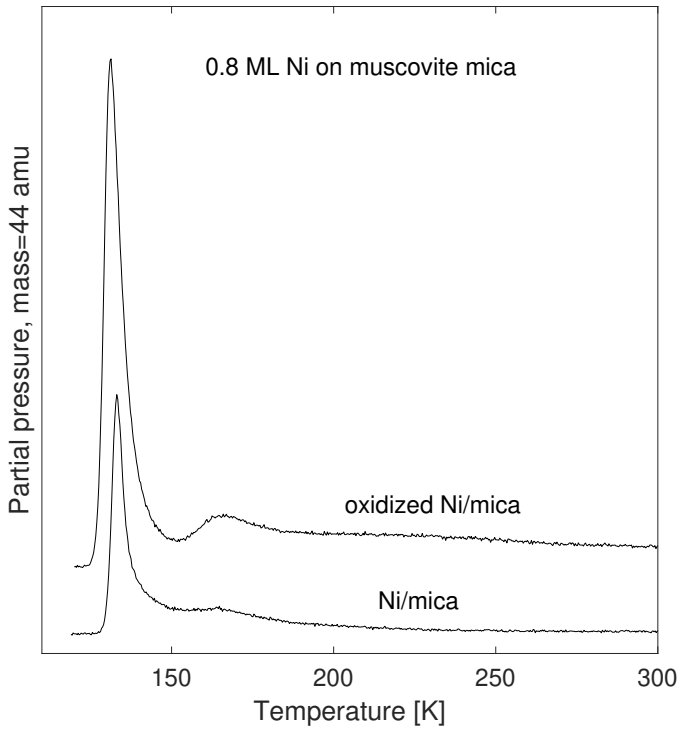

Figure 6. TPD of CO_2 (mass 44 amu) from 0.8 ML effective Ni coverage on mica. The top curves show desorption from oxidized Ni/mica, and the bottom curves show desorption from metallic Ni/mica.

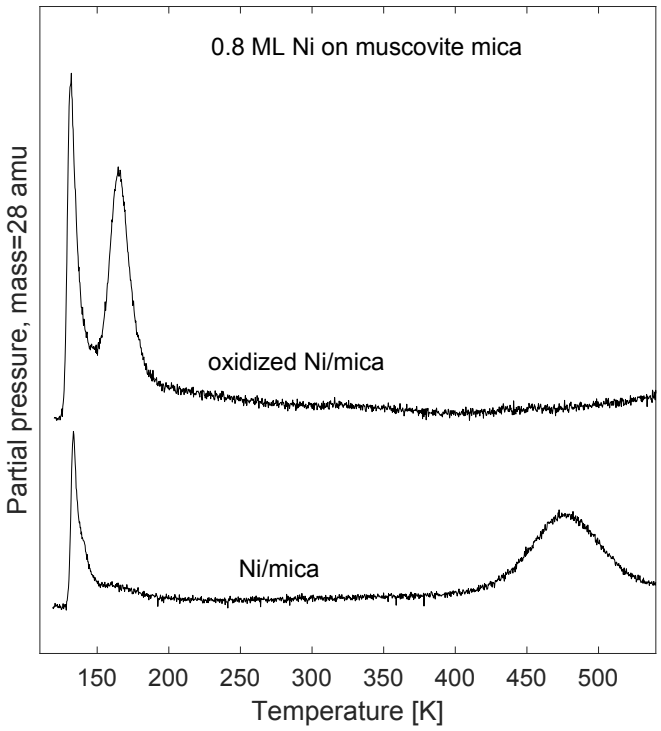

Figure 7. TPD of CO (mass 28 amu) from 0.8 ML effective Ni coverage on mica. The top curves show desorption from oxidized Ni/mica, and the bottom curves show desorption from metallic Ni/mica.

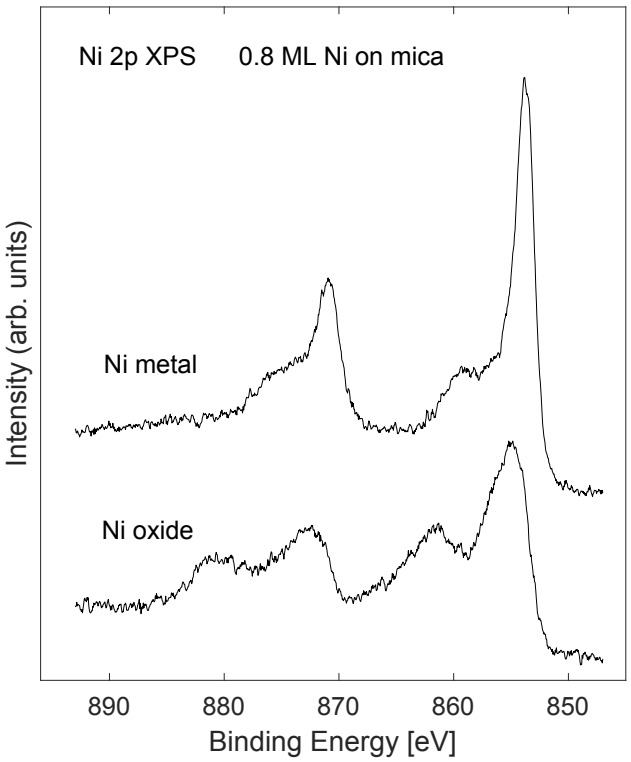

Figure 8. XPS of Ni 2p core levels for metallic and oxidized Ni/mica.

sorption sites are available in the oxidized samples. The desorption temperatures are near equal. The simultaneously obtained desorption of CO indicates physisorption (desorption at 166 K) on the oxidized sample and chemisorption (desorption at 479K) on the metallic sample.

There exist a controversy in the literature regarding dissociation of CO_2 on metal surfaces [18]. Chemisorption and dissociation of carbon monoxide are well documented on doped Ni surfaces [20, 21]. Physisorption of CO_2 is observed on all Ni surfaces at low temperatures. When the temperature increases the molecule may chemisorb. The reactivity of Ni systems follow the trend Ni(110) > Ni(100) > Ni(111), being more reactive for an open surface [9]. Evidence for dissociation of CO_2 on the supported Ni nano-structures was not found in the present work. The distinct CO desorption peaks that were observed in Fig.3 show the large affinity to carbon monoxide of the Ni nano-structures. An early conjecture of dissociation of CO_2 was dismissed since similar mass = 28 amu peaks were observed in the absence of exposure to carbon dioxide, which shows that adsorption of CO takes place during the experiment from the ambient pressure in the vacuum chamber in which the base pressure is about $1{\cdot}10^{-10}$ mbar. This leads to the suggestion that observation of CO desorption peaks may not be taken as proof of dissociation of CO_2 in Ni systems.

Due to the low desorption temperature it may be argued that the CO peak at 166 K is caused by physisorption in the case of the oxidized Ni/mica sample.

The observation, see Fig.2, that the CO_2 physisorption peak is located about 20 K at higher temperature for the 2.0 ML Ni sample as compared to the 0.8 ML Ni sample is argued to be related to the presence of Ca in the 2.0 ML sample, as shown in Fig.5. The Ca content stems from variations in the muscovite mica substrates. Most mica samples were found to contain negligible amounts of calcium. The work functions of Ca and Ni are about 2.7 and 5.0 eV, respectively [16]. The physisorption peak is controlled by Van der Waals forces, which are induced dipole-dipole interactions that are sensitive to work function changes [17, 18]. Lower work function implies stronger physisorption bonds. By comparison, the CO chemisorption peak near 500 K, seen in Fig.3, is not similarly affected. If this interpretation is correct, it may indicate that CO_2 physisorption takes place near the Ni-mica interface. In contrast to the work of adsorption of CO on Ni nano-structures on mica where strong nano-structure size dependence was observed, desorption of CO_2 does not seem to depend strongly on the amount of Ni on the surface of the mica substrate. This may be due to the observation of a very low tendency of chemisorption of CO_2 on these surfaces.

5. Conclusions

Thermal desorption spectra have shown that predominantly physisorption of carbon dioxide was observed on metallic and oxidized Ni nano-structures supported on muscovite mica. Only weak chemisorption features were observed at temperatures up to room temperature for both metallic and oxidized Ni nano-structures. Dissociation of CO_2 was not observed on the metallic nor oxidized Ni samples. Near a factor of two more CO_2 was seen to be adsorbed on the oxidized Ni nano-structures as compared to the metallic ones. The Ni nano-structures were found to be very reactive towards CO adsorption from the ambient pressure in the vacuum chamber, based on the observation of a CO desorption peak even in the absence of CO_2 or CO exposure. Desorption of CO_2 was found to depend only weakly on the amount of Ni on the muscovite mica substrates in the mono-layer thickness regime.

Acknowledgements

This work was supported by the Research Council of Norway (RCN) under project no. NFR 250728.

References

[1] K.S. Lackner, *A Guide to CO_2 Sequestration.* Science 300 (2003), pp.1677-1678. doi:10.1126/science.1079033

[2] C. Song, *Global challenges and strategies for control, conversion and utilization of CO_2 for sustainable development involving energy, catalysis, adsorption and chemical processing.* Catalysis Today 115 (2006), pp.2-32. doi:10.1016/j.cattod.2006.02.029

[3] T. Sakakura, J.-C. Choi, and H. Yasuda, *Transformation of Carbon Dioxide.* Chemical Reviews 107 (2007), pp.2365-2387. doi:10.1021/cr068357u

[4] O.V. Krylov and A.Kh. Mamedov, *Heterogeneous catalytic reactions of carbon dioxide.* Russian Chemical Reviews 64 (1995), pp.877-900. doi:10.1070/RC1995v064n09ABEH000182

[5] E. Vesselli, L. De Rogatis, X. Ding, A. Baraldi, L. Savio, L. Vattuone, M. Rocca, P. Fornasiero, M. Peressi, A. Baldereschi, R. Rosei, and G. Comelli, *Carbon Dioxide Hydrogenation on Ni(110).* Journal of the American Chemical Society 130 (2008), pp.11417-11422. doi:10.1021/ja802554g

[6] J. Nerlov and I. Chorkendorff, *Promotion through gas phase induced surface segregation: methanol synthesis from CO, CO_2 and H_2 over Ni/Cu(100).* Catalysis Letters 54 (1998), pp.171-176. doi:10.1023/A:1019033517855

[7] X. Ding, L. De Rogatis, E. Vesselli, A. Baraldi, G. Comelli, R. Rosei, L. Savio, L. Vattuone, M. Rocca, P. Fornasiero, F. Ancilotto, A. Baldereschi, and M. Peressi, *Interaction of carbon dioxide with Ni(110): A combined experimental and theoretical study.* Physical review B 76 (2007), pp.195425. doi:10.1103/PhysRevB.76.195425

[8] H.-J. Freund and M.W. Roberts, *Surface chemistry of carbon dioxide.* Surface Science Reports 25 (1996), pp.225-273. doi:10.1016/S0167-5729(96)00007-6

[9] S.-G. Wang, D.-B. Cao, Y.-W. Li, J. Wang, and H. Jiao, *Chemisorption of CO_2 on Nickel Surfaces.* The Journal of Physical Chemistry B 109 (2005), pp.18956-18963. doi:10.1021/jp052355g

[10] K.W.B. Hunvik, A. Støvneng, B. Pacáková, and S. Raaen, *CO desorption from nickel-decorated muscovite mica.* Applied Surface Science 490 (2019), pp.430-435. doi:10.1016/j.apsusc.2019.06.073

[11] R. A. van Santen and M. Neurock, *Molecular Heterogeneous Catalysis.* Wiley-VCH (2006), isbn: 3-527-29662-X

[12] G.C. Bond, *Small particles of the platinum metals.* Platinum Metals Review 19 (1975), pp.126-134.

[13] C.A. de Araujo Filho and D.Y. Murzin, *A structure sensitivity approach to temperature programmed desorption.* Applied Catalysis A, General 550 (2018), pp.48-56. doi:10.1016/j.apcata.2017.11.001

[14] S. Raaen and K.W.B. Hunvik, *Non-activated adsorption of methane on nickel surfaces induced by reduced work function.* Applied Surface Science (2020).

[15] S. Hüfner and G.K. Wertheim, *Multielectron effects in the XPS spectra of nickel.* Physics Letters A 51 (1975), pp.299-300. doi:10.1016/0375-9601(75)90457-0

[16] E.A. Mechtly, *Reference Data for Engineers (Ninth Edition). 4 - Properties of Materials.* Newnes, Woburn (2002). isbn:978-0-7506-7291-7. doi:10.1016/B978-075067291-7/50006-6

[17] E. Hult, P. Hyldgaard, J. Rossmeisl, and B.I. Lundqvist, *Density-functional calculation of van der Waals forces for free-electron-like surfaces.* Physical Review B (2001), pp.195414. doi:10.1103/PhysRevB.64.195414

[18] U. Burghaus, *Surface chemistry of CO_2. Adsorption of carbon dioxide on clean surfaces at ultrahigh vacuum.* Progress in Surface Science 89 (2014), pp.161-217. doi:10.1016/j.progsurf.2014.03.002

[19] G. Illing, D. Heskett, E.W. Plummer, H.-J. Freund, J. Somers, Th. Lindner, A.M. Bradshaw, U. Buskotte, M. Neumann, U. Starke, K. Heinz, P.L. De Andres, D. Saldin, and J.B. Pendry, *Adsorption and reaction of CO_2 on Ni110: X-ray photoemission, near-edge X-ray absorption fine-structure and diffuse leed studies.* Surface Science 206 (1988), pp.1-19. doi:10.1016/0039-6028(88)90010-6

[20] W. Xie, W. Sun, W. Chu, C. Jiang, and Y. Xue, *Investigation of the doped transition metal promotion effect on CO_2 chemisorption on Ni (111).* Applied Surface Science 258 (2012), pp.6239-6245. doi:10.1016/j.apsusc.2012.03.001

[21] F. Besenbacher, I. Chorkendorff, B.S. Clausen, B. Hammer, A.M. Molenbroek, J.K. and Nørskov, and I. Stensgaard, *Design of a Surface Alloy Catalyst for Steam Reforming.* Science 279 (1998), pp.1913-1915. doi:10.1126/science.279.5358.1913

[22] D. Nečas and P. Klapetek, *Gwyddion: an open-source software for SPM data analysis.* Central European Journal of Physics 10 (2012), pp.181-188. doi:10.2478/s11534-011-0096-2

[23] Haugstad, G., *Atomic Force Microscopy. Ch.8 Data Post-Processing and Statistical Analysis.* John Wiley &Sons, Ltd (2012), pp.379-399. doi:10.1002/9781118360668.ch8

[24] K. Godin, C. Cupo, and E.-H. Yang, *Reduction in Step Height Variation and Correcting Contrast Inversion in Dynamic AFM of WS 2 Monolayers.* Scientific Reports 7 (2017), pp.1-11. doi:10.1038/s41598-017-18077-4

[25] R. Dong, and L.E. Yu, *Investigation of Surface Changes of Nanoparticles Using TM-AFM Phase Imaging.* Environ. Sci. Technol. 37 (2003), pp.2813-2819. doi:10.1021/es034071k

[26] A. Kühle, A.H. Sorensen, J.B. Zandbergen, and J. Bohr, *Contrast artifacts in tapping tip atomic force microscopy.* Applied Physics A 66 (1998), pp.S329-S332. doi:10.1007/s003390051156

[27] P. Klapetek, M. Valtr, D. Nečas, O. Salyk, and P. Dzik, *Atomic force microscopy analysis of nanoparticles in non-ideal conditions.* Nanoscale Research Letters 6 (2011), pp.514. doi:10.1186/1556-276X-6-514